



## ORIGINAL ARTICLE

# Dye removal, antibacterial properties, and morphological behavior of hydroxyapatite doped with Pd ions

Zehbah Ali Al-Ahmed<sup>a</sup>, Najlaa S. Al-Radadi<sup>b</sup>, M.K. Ahmed<sup>c,\*</sup>, Kamel Shoueir<sup>d</sup>, Maged El-Kemary<sup>d</sup>

<sup>a</sup> College of Art and Sciences – Dhahran Aljounb, King Khalid University, Saudi Arabia

<sup>b</sup> Chemistry Department, Faculty of Science, Taibah University, P.O. Box 30002, Al-Madinah Monawara 14177, Saudi Arabia

<sup>c</sup> Department of Physics, Faculty of Science, Suez University, Suez, Egypt

<sup>d</sup> Institute of Nanoscience & Nanotechnology, Kafrelsheikh University, 33516 Kafrelsheikh, Egypt

Received 21 July 2020; accepted 22 September 2020

Available online 8 October 2020

## KEYWORDS

Pd;  
Hydroxyapatite;  
Antibacterial;  
Dye removal;  
Methylene blue

**Abstract** Hydroxyapatite (HAP) containing different contents of palladium (Pd) ions were synthesized using the co-precipitation method. The structural and morphological properties of the as-synthesized compositions were investigated using XRD and FESEM. The *c/a* increased from 0.728 to 0.733 with the lowest and highest contributions of Pd(II), respectively. Furthermore, the morphological features were investigated using FESEM. It was illustrated that Pd-HAP was formed as agglomerated as rod shapes with dimensions in the range of 63.4–110.3 nm for no Pd additions, and the size was reduced reaching 43.4–70.5 nm for the highest Pd contribution. Besides, the maximum height of the roughness ( $R_t$ ) grew from 183.6 up to 236.5 nm for the lowest and highest Pd (II). Besides, the obtained specific surface area was around 28.3, 42.0, and 63.4 m<sup>2</sup>/g for 0.0Pd-HAP, 0.6Pd-HAP, and 1.0Pd-HAP, respectively. The antibacterial activity was examined against both *Escherichia coli* (*E-coli*) and *Staphylococcus aureus* (*S. aureus*), and it obvious that the activity was enhanced upon Pd content. The inhibition zone was increased from no sensitivity reaching  $4.3 \pm 0.9$  and  $4.5 \pm 0.8$  mm for no Pd and the highest one, respectively. The removal efficiency of dyes was examined for methylene blue (MB) and it was shown that after 120 min of irradiation, the removal efficiency reached around 86.4% for the highest contribution of Pd. The pseudo-first-order constant ( $K_{app}$ ) increased from 0.0032 to 0.0179 min<sup>-1</sup>. The recyclability of Pd-HAP denoted that

\* Corresponding author.

E-mail address: [m.khalaf@sci.suezuni.edu.eg](mailto:m.khalaf@sci.suezuni.edu.eg) (M.K. Ahmed).

Peer review under responsibility of King Saud University.



Production and hosting by Elsevier

removal efficiency decreased to 5.65, 8.14, 6.24, 8.76, and 10.2% for different contents of Pd(II) after 6 cycles.

© 2020 Published by Elsevier B.V. on behalf of King Saud University. This is an open access article under the CC BY-NC-ND license (<http://creativecommons.org/licenses/by-nc-nd/4.0/>).

## 1. Introduction

The rapid industrial development in recent decades has caused numerous environmental problems. For instance, dyes production for printing, food packing, cosmetics, textiles, and pharmaceuticals is suggested to be directly discharged into rivers and drinking water resources (Wu et al., 2020b; Zou et al., 2020; Zhu et al., 2020; Zheng et al., 2020). It could be reported that around 100 tons of dyes are release into drinking water annually (Piri et al., 2019). Besides, the progression of a population due to the great expansion of health care systems globally has exhausted the limited sources of drinking water (Zhao et al., 2020b; Zhang et al., 2020b). Dyes such as congo red, methylene blue (MB), acid Blue 121, and blue 60 are difficult to be degraded in the normal conditions (Shoueir, 2020). The extreme exposure to these dyes may cause harm to living cells including kidney, liver, and even cancer cell initiation (Zhang et al., 2020a; Yao et al., 2020).

In addition to this, excessive use of antibiotics to fight bacterial infections may lead to a formation of super-bacteria, besides the pharmaceutical released towards the water. Therefore, the suggestion of an alternative antibacterial agent to avoid traditional antibiotics is a vital demand to develop a care health system (Xu et al., 2020; Wang et al., 2020c). For instance, rifampicin which is a widely used antibiotic against tuberculosis, however, it has been reported to be sued in large quantities for aquaculture. Therefore, around 20–30% of their quantities absorbed by fish, while the rest discharged to the environment.

Intensive efforts have been examined to develop facile methods for water treatment involving adsorption, electrolysis, membrane filtration, photocatalysis, chemical oxidation (Zhang et al., 2020b), electrochemical treatment, and flocculation precipitation (Wu et al., 2020b). The adsorption is suggested to be one of the widely utilized techniques for dye removal owing to its availability, low cost, high efficiency, and its ability to be applied on a large scale (Wang et al., 2020a).

Hydroxyapatite [HAP:  $\text{Ca}_{10}(\text{PO}_4)_6(\text{OH})_2$ ] is a bioceramics substance and it resembles the main inorganic constituent of bone and teeth through vertebrates' tissues. Therefore, it has been used for numerous applications upon its high biocompatibility, low toxicity, bioactivity, and osteoconductivity. These applications include gas senes, catalysis, adsorption, drug delivery, cancer treatment, tissue engineering, and fertilizers (Reeta Mary et al., 2018).

Furthermore, HAP possesses high chemical and thermal stability, cheap to be synthesized, low water-soluble, besides its ionic exchange and adsorption affinity. Concerning adsorption behavior, it has been used for the separation of biomolecules, water filtration, heavy metal removal, soil remediation. It could be mentioned that the cationic and anionic capacity of HAP relies on its structural configuration (Wang et al., 2020b, 2017a). The structural resilience of HAP allows ions to replace Ca or P sites, individually or simultaneously (Gore et al., 2017; Wang et al., 2015). This modification introduces additional properties of HAP including higher biodegradation rate and higher bioactivity, besides extrinsic behaviors such as antibacterial and anti-cancer in case of ionic substitutions of Ag, Se, Pt...etc. (Shoueir et al., 2020b; Menazea et al., 2020; Al-Wafi et al., 2020).

It might be reported that Xi Chen et al. has investigated the removal effectiveness of HAP modified with xanthan gum. The results showed that the maximum adsorption capacity achieved around 769 mg/g of MB from aqueous solution (Chen et al., 2020). On the other hand, Wei et al. studied the ability of humic acid-modified HAP for MB removal, and they optimized the conditions as adsorbent

of 2.2 g/L, exposure time of 8 h and MB concentration of 85 mg/L and the removal effectiveness reached 100% (Shoueir, 2020). Moreover, J. S. da Silva et al. examined the discoloration efficiency of HAP/ $\alpha$ - $\text{AgVO}_3$  for MB and they found that the optimum conditions of around 22.5 wt% HAP/ $\alpha$ - $\text{AgVO}_3$  have shown a removal activity (85%) after 60 min of continuous exposure for UV irradiation (da Silva et al., 2020). While I. R. Mary et al. investigated the removal efficiency of HAP spherical nanoparticles and the results displayed that the degradation effectiveness reached about 75% after 240 min of exposure to UV irradiation (Reeta Mary et al., 2019). Moreover, I. R. Mary et al. fabricated HAP nested bundles for dye removal purposes, and the results showed that the removal efficiency was around 77–91% after 210 min of exposure to UV irradiation (Reeta Mary et al., 2018).

It was reported that Pd(II) possesses a great catalytic activity, therefore, it was investigated to be used as a catalytic agent for the Suzuki coupling reaction as studied by Yilmaz et al. (2020) and Wang and Bai (2020). However, the accepted level of Pd(II) within drinking water should not exceed 5–10 ppm upon the evaluation of the European Agency (Zhao et al., 2020a).

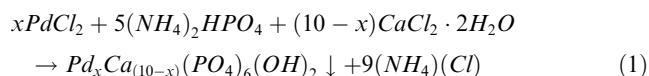
Furthermore, Xu et al. have used rGO@Fe/Pd hybrid nanoparticles for rifampicin removal from aqueous solutions and the results displayed that the removal efficiency reached about 89.0%, while Pd nanoparticles acted as catalytic agent (Xu et al., 2020). Moreover, Mansour et al. studied the anti-cancer effect of co-doped Pd/S into HAP, and the  $\text{IC}_{50}$  was estimated to be around 1.22 mg/mL against the A549 assay (Mansour et al., 2018).

Consequently, this work aims to develop HAP with different contents of Pd(II) ions. The obtained as-synthesized composites could be investigated upon their structural, morphological features, besides their adsorption-desorption behavior. Also, their activity to remove MB from aqueous solutions will be investigated, as well as the antibacterial activity.

## 2. Materials and methods

### 2.1. Synthesis of Pd-HAP

Calcium chloride dihydrate [ $\text{CaCl}_2 \cdot 2\text{H}_2\text{O}$ ], diammonium hydrogen phosphate [ $(\text{NH}_4)_2\text{HPO}_4$ ], and palladium chloride [ $\text{PdCl}_2$ ] were purchased from LOBA, India, and they were utilized without further purifications. Then HAP was prepared using the co-precipitation method using appropriate molar ratios as the following equation:



where  $x = 0.0, 0.4, 0.6, 0.8$  and  $1.0$ .

In summary, different contributions of [ $\text{CaCl}_2 \cdot 2\text{H}_2\text{O}$ ] were used including 0.5, 0.48, 0.46, 0.44 and 0.42 M to be dissolved in 100 mL of distilled water, individually and 0.02, 0.04, 0.06 or 0.08 M of  $\text{PdCl}_2$  were added into the accompanied Ca solution. On the other hand, 0.3 M of [ $(\text{NH}_4)_2\text{HPO}_4$ ] was prepared in 100 mL as a fixed solution for each Ca. Then, (P) solution was added drop wisely into the analog (Ca + Pd) solution, whereas continuous stirring is working. The pH value was kept at  $11.0 \pm 0.1$ . After 1 h of stirring, the solutions were aged for

24 h for precipitation, then they were washed using distilled water, and dried 50–60 °C.

## 2.2. Characterizations

X-ray diffraction (XRD) patterns were recorded on a (Pertpro, Cu  $k_{\alpha 1}$  radiation,  $\lambda = 1.5404 \text{ \AA}$ , 45 kV, 40 mA, USA) diffractometer. The taken range at  $2\theta = 5\text{--}60^\circ$  and the average crystalline size of different Pd content was calculated using the well-known Debye–Scherrer equation (Mansour et al., 2017c). To confirm the functionality of Pd-HAP, the FT-IR spectrum (Model no. AUP1200343) was used, 500–4000  $\text{cm}^{-1}$  is the controlled range. Thermal stability of the 0.0Pd-HAP, 0.6Pd-HAP, and 1.0Pd-HAP was determined in the temperature range of 20–1000 °C (DTG 60, Shimadzu), and the thermal analysis of the samples was performed in an  $\text{N}_2$  inert gas atmosphere with a heating rate of 5 °C/min. The surface area was measured by BET analysis (Micromeritics 3Flex equipment Tristar II 3020). The surface texture and roughness parameters were measured using a field emission scanning electron microscope (FESEM) and scan the surface roughness with an operating voltage fixed at 20 kV (model: FEG250 - QUANTA, Netherlands). Micrographs of different content of Pd-HAP were obtained using FESEM before culturing the cell line and treated using Gwyddion 2.45 software to scan their roughness (Mansour et al., 2017b). 3D images were processed for each composition and the resolution was maintained at  $16,000 \times 1020$  pixels. The edges of the micrograph have been removed to avoid excessive borders. Therefore, the dependence of the roughness parameters on the changes in the compositions was evaluated by the program itself in (nm).

## 2.3. Antibacterial activity

The performance of Pd-HAP as antibacterial was studied towards gram-positive (*S. aureus*) and in gram-negative (*E. coli*) under the same conditions. The recommended initial concentration is 50 mg/ml of each one to be analyzed. The inhibition zone was measured after one day of incubation at 37 °C in the aid of visible-light illumination.

## 2.4. Photocatalytic set-up

A working solution to verify the MB extraction process was set at 5 mg/L of MB. Then, about 50 mg of the Pd-HAP powder phase was added to each MB beaker containing (10 mL of MB) separately at room temperature. The lighting system used here is a visible light spectrum (100 W) in a sealed box. After illumination, 3 mL of the catalyst/MB solution was removed by centrifugation to measure with a spectrophotometer at measurable time intervals. The ( $\eta$  %) is estimated via the expression (Abdelbar et al., 2018; Abou-Zeid et al., 2018; Salama et al., 2018; Ramadan, 2019):

$$\eta(\%) = \left( \frac{C_0 - C_t}{C_0} \right) \times 100 \quad (2)$$

$C_0$  and  $C_t$  are initial and optimal concentration at a specific time (t). The spectra were registered on a double beam spectrophotometer (Shimadzu UV-1208 model). After the deple-

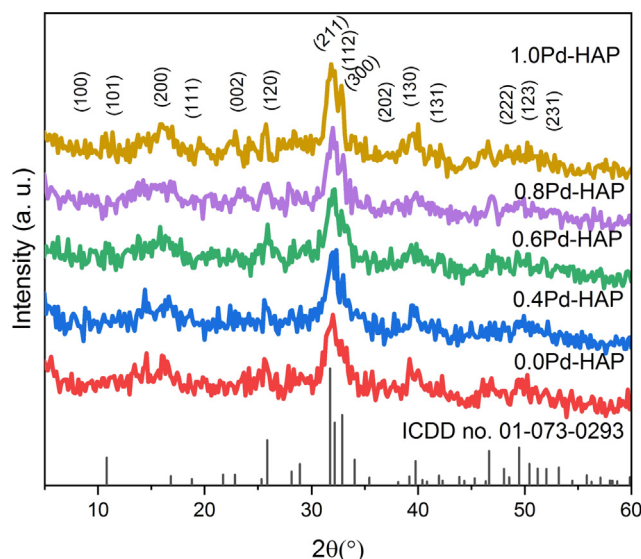


Fig. 1 XRD patterns of Pd-HAP at different contents of Pd(II).

tion of MB, the precipitated powder was centrifuged to repeat the experiment to examine the recyclability.

## 3. Results and discussion

### 3.1. Structural investigation

The XRD patterns were used to investigate the phase composition of the powder phase of Pd-HAP, and it was illustrated in Fig. 1 that HAP seems to be crystallized in a single-phase upon the ICDD card no (01-073-0293). The diffraction peaks indicated that composition has a hexagonal symmetry accruing to the space group of  $P6_3/m$ . The fact that there are no other phases that were detected through the XRD patterns might indicate that Pd(II) ions have been successfully trapped into HAP lattice.

The crystallite size upon Scherrer's equation was reported in Table 1, displays a decreasing trend with rising the content of Pd(II) starting from 36.7 nm at no additional Pd reaching to 18.6 nm at the highest contribution of Pd(II). Lattice parameters seem to be changed considerably upon the variation of Pd(II) contribution within HAP structure. The a-axis decreases from 9.447 to 9.412, 9.389, 9.361, and 9.368 Å, while the c-axis fluctuates starting from 6.875, 6.885, 6.871, 6.882 and 6.866 Å for 0.0Pd-HAP, 0.4Pd-HAP, 0.6Pd-HAP, 0.8Pd-HAP, and 1.0Pd-HAP, respectively. Moreover, c/a ratio increases when Pd is present with respect to no Pd, which indicates that HAP crystals tend to grow in the c-axis.

The two sites of Ca(II) are two perspective crystallographic positions to be replaced partially with Pd(II) ions. The coordination of Ca(1) is shaped as a tricapped trigonal prism and possesses the main effect towards the c-axis, while the Ca(2) is configured in a distorted octahedron and affects into a-axis (Jiang et al., 2002;66). The ionic substitution of Pd(II) into either Ca(1) or Ca(2) induces a crystallographic distortion due to the difference in both ionic radii and the folds coordination between Ca(II) and Pd(II). The ionic radius of Pd(II) is around ions (0.86 Å), while it tends to be larger for Ca(II) with a value of (0.99 Å). The Pd(II) ion possesses a

**Table 1** The crystallographic data of Pd-HAP including crystal size, lattice parameters, and theoretical density upon Pd(II) contents.

Composition	Crystal size (nm)	lattice parameters		c/a	V (Å <sup>3</sup> )	D <sub>x</sub> (g/cm <sup>3</sup> )
		a (Å)	c (Å)			
0.0Pd-HAP	36.7	9.447	6.875	0.728	531.363	3.140
0.4Pd-HAP	30.1	9.412	6.885	0.732	528.233	3.158
0.6Pd-HAP	28.4	9.389	6.871	0.732	524.564	3.180
0.8Pd-HAP	25.8	9.361	6.882	0.735	522.225	3.195
1.0Pd-HAP	18.6	9.368	6.866	0.733	521.815	3.197

coordination number of (6), while the available coordinations for Ca(II) are (7) and (9) for Ca(2) and Ca(1), respectively. Therefore, to minimize lattice distortion, Pd(II) is hypothesized to replace Ca(2) sites rather than Ca(1). Due to the crystallographic position of Ca(2) through the ab plan, it might provoke a distortion in a-axis, therefore, the variation in values of a-axis matches well with the hypothetical notes. Furthermore, it was reported that the carbonate (CO<sub>3</sub><sup>2-</sup>) group tends to replace phosphate (B type) or hydroxyl (A-type) sites individually or simultaneously (AB type). However, the AB type might be considered as the most energetically preferred crystallized orientation of HAP crystal upon Wu et al. (2020a). The theoretical density increases from 3.140 to 3.197 g/cm<sup>3</sup> for the lowest and the highest Pd(II) contents owing to the addition of molar mass of heavy ions into the calculations.

### 3.2. FTIR

The FTIR spectra of the Pd-HAP compositions are illustrated in Fig. 2, whereas the characteristic bands are reported in Table 2. The bands of 472.8 cm<sup>-1</sup> indicate the bending vibrational mode (ν<sub>2</sub>) of O–P–O, while the bands of 567.5 and 603.4 cm<sup>-1</sup> refer to the formation of bending mode (ν<sub>4</sub>) belong to PO<sub>4</sub><sup>3-</sup> (Mansour et al., 2015; Ahmed et al., 2014). The band of 1038.4 cm<sup>-1</sup> is assigned to the asymmetric stretching (ν<sub>3</sub>) of PO<sub>4</sub><sup>3-</sup> (Ahmed et al., 2019b, 2018). Furthermore, the bands of

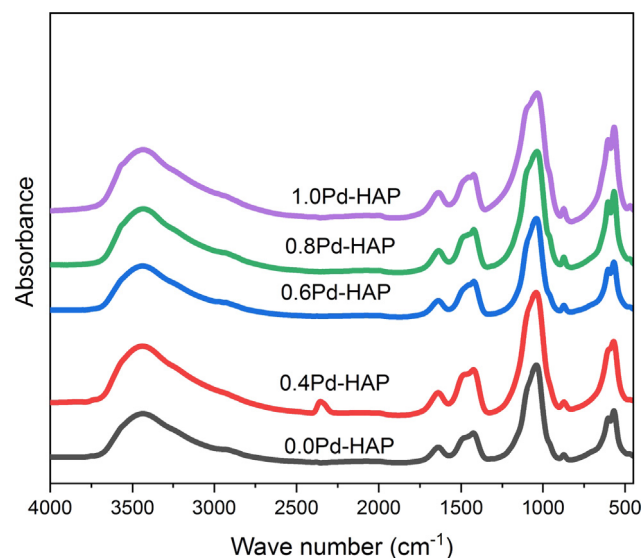


**Fig. 2** FTIR spectra of HAP modified with different additive concentration of Pd(II).

1639.3 and 3844.3 cm<sup>-1</sup> indicate the absorbed OH<sup>-</sup> groups on the lattice surface. On the other hand, the bands of 874.3, 1427.3, and 1456.4 cm<sup>-1</sup> indicate the presence of vibrations of ν<sub>2</sub> and ν<sub>3</sub> belonging to CO<sub>3</sub><sup>2-</sup> groups, respectively (Ahmed et al., 2020c, 2019a; Afifi et al., 2020). The high affinity of CO<sub>3</sub><sup>2-</sup> ions to be absorbed through HAP structure among the synthesis process via the CO<sub>2</sub> from the ambient atmosphere, may introduce a facile and spontaneous way for an ionic replacement. This ionic substitution promotes crystallographic disordering within the unit cell, and thus plunge the crystallographic orientation through the lattice. The deterioration of lattice regularity induces a high rate of degradation and lowering of thermal and chemical stability, besides encouraging chemical activity towards the atomic milieu.

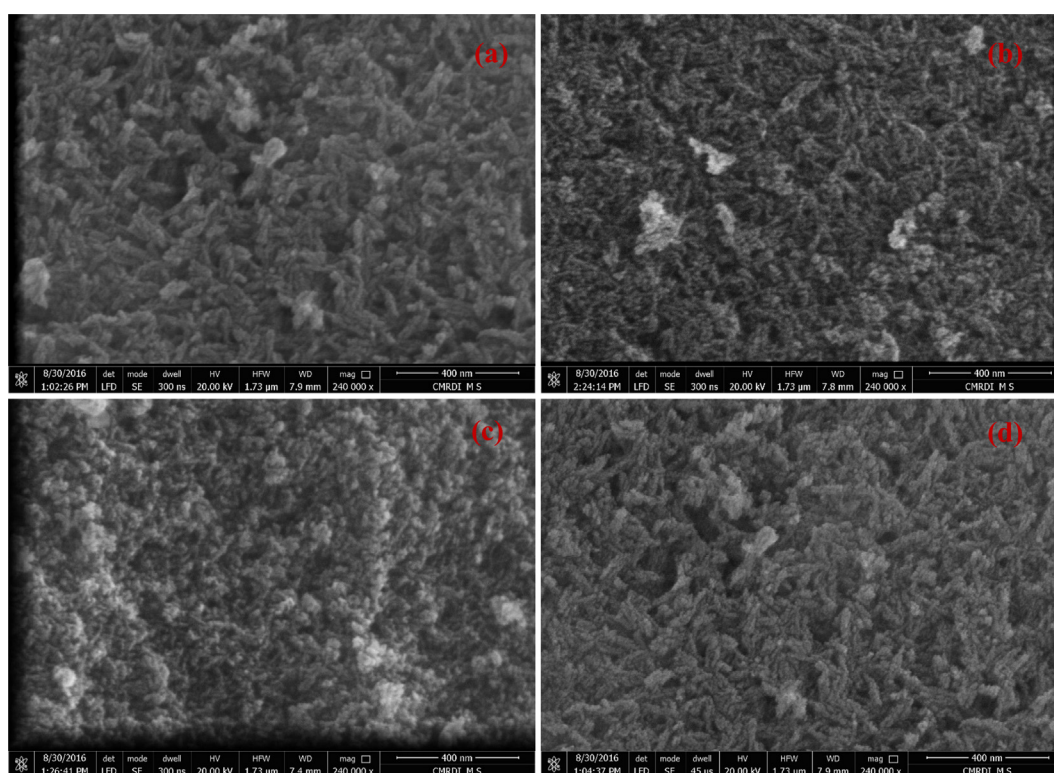
### 3.3. Morphological features

The surface morphology of Pd-HAP depends strongly on the components' variation as obvious in Fig. 3(a)–(d). At zero addition of Pd(II), pristine HAP seems to be formed in agglomerated rod shapes with lengths in the range of 63.4–110.3 nm, and diameters about 8.3 nm. The rods are distributed in non-oriented grains, while porosity content tends to be high. Fig. 3(b) shows that the surface of 0.4Pd-HAP was configured as aggregated rods with dimensions of (44.1–59.7) × 9.1 nm for length × diameter, respectively. The composition of 0.6Pd-HAP was formed with rods of lengths around 49.1–100.4 nm and diameters of 5.1 nm. The roughness tends to be higher, while porosity is lower than the former compositions. The highest contribution of Pd(II) into HAP seems to be shaped as a rough rod with lengths of 43.4–70.5 nm and diameters of 6.5 nm, and porosity content seems to be higher than the former ones. It could be noticed that the grain size of Pd-HAP is reduced with the rising of Pd(II) contribution. This trend is assigned to the crystallographic disordering that is provoked upon the additional ions. Therefore, controlling ionic substitution is a good tool to control shapes and grains size distribution.

The progression of surface roughness of Pd-HAP is shown in Fig. 4(a)–(d), while the roughness parameters are reported in Table 3. It is noticed that the roughness average (R<sub>a</sub>) increases from 21.7 reaching 35.3 nm upon the substitution contribution. The root means square roughness (R<sub>q</sub>) seems to follow the behavior of (R<sub>a</sub>). On the other hand, the maximum height of the roughness (R<sub>t</sub>) displays higher values than the maximum roughness valley depth (R<sub>v</sub>) for the conjugated compositions. The roughness behavior contains two main contributors: peaks and notches. While R<sub>t</sub> refers to the peaks, R<sub>v</sub> denotes to the notches. Therefore, the higher values of R<sub>t</sub> implies that the Pd-HAP seems to be conspicuous, which intro-

**Table 2** Characteristic bands of Pd-HAP at different contents of Pd(II) ions.

0.0Pd-HAP	0.4Pd-HAP	0.6Pd-HAP	0.8Pd-HAP	1.0Pd-HAP	Assignment	Ref
472.8	—	—	473.2	471.2	$\nu_2$ of O–P–O	(Ahmed et al., 2014; Lukić et al., 2014)
567.5	571.2	—	568.2	567.4	$(\nu_4)$ of $\text{PO}_4^{3-}$	(Tang et al., 2014; Wang et al., 2017b; Duta et al., 2017)
603.4	—	604.3	602.3	603.5	$(\nu_4)$ of $\text{PO}_4^{3-}$	(Mansour et al., 2017b, 2017a; El-dek et al., 2017)
874.3	871.5	871.6	872.5	873.5	$\nu_2$ of $\text{CO}_3^{2-}$	(Lukić et al., 2014; Wang et al., 2016)
1038.4	1042.4	1039.5	1038.4	1037.5	$(\nu_3)$ of $\text{PO}_4^{3-}$	(Fadeeva et al., 2012)
1427.3	1426.5	1424.5	1424.7	1425.3	$\nu_3$ of $\text{CO}_3^{2-}$	(Lukić et al., 2014; Niakan et al., 2015)
1456.4	1454.5	1454.7	1455.8	1455.5	$(\nu_3)$ of $\text{CO}_3^{2-}$	(Wang et al., 2018; Zhang et al., 2016)
1639.3	1638.4	1638.5	1637.5	1636.4	Absorbed water	(Lukić et al., 2014; Toyama and Kameda, 2013)
2074.5	2074.7	2077.4	2077.6	2076.8	Overtone of $\text{PO}_4^{3-}$	(Ahmed et al., 2014)
3437.2	3441.4	3440.3	3438.5	3436.5	Stretching of	(Lukić et al., 2014; Toyama and Kameda, 2013)
3844.3	3846.6	3845.4	3845.8	3846.7	$\text{OH}^-$	

**Fig. 3** FESEM micrographs of as-synthesized Pd-HAP; (a) 0.0Pd-HAP, (b) 0.4Pd-HAP, (c) 0.6Pd-HAP and (d) 1.0Pd-HAP.

duce a physical way to interact with the ambient atmosphere (Ahmed et al., 2020b, 2020a, 2020f). The adhesion with the surrounding environment is a vital property to activate the serial interaction for versatile applications including drug delivery, antibacterial agency, and water filtration (Ahmed et al., 2020b, 2020a, 2020c). Consequently, the roughness manipulation, and thus the activity is controlled via the compositional tailoring.

### 3.4. Thermal stability

The thermogravimetric analysis has been done for Pd-HAP at different concentrations of Pd(II) up to 1000 °C in ambient air as shown in Fig. 5. It is noticed that the rate of weight loss

seems to be high for all composition starting from room temperature (R. T.) up to around 70 °C, whereas the compositions lost about 3.7% of their initial weights. The weight loss in this stage is referred to as the release of the absorbed water molecules. Therefore, all curves seem to be identical in the first stage.

The second stage continues upon 418 °C, and obvious that the loss rate increases significantly upon the content of Pd(II), where the powdered compositions of 0.0Pd-HAP, 0.6Pd-HAP, and 1.0Pd-HAP loss around 9.2, 15.7, and 14.6% from their weights at 418 °C, respectively. In this stage, the compositions tend to be degenerated to release hydroxyl ions, which is the initial stage before transforming to calcium oxide phases. The presence of Pd(II) through the crystal provokes high

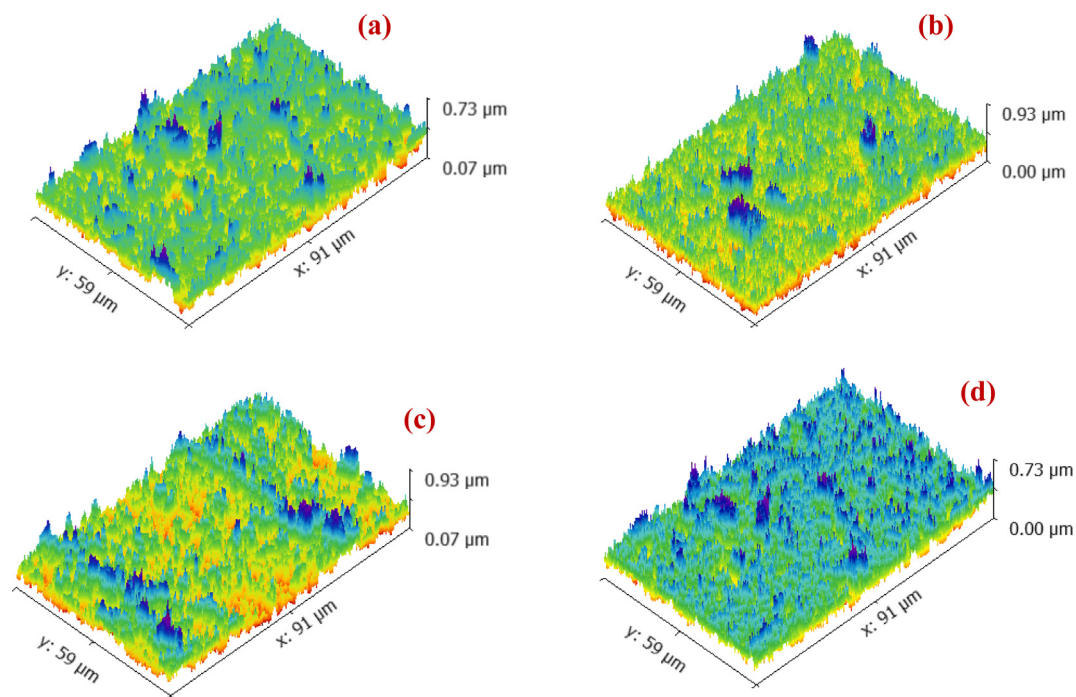


**Fig. 4** Development of surface roughness upon the variation of Pd(II) contributions through Pd-HAP; (a) 0.0Pd-HAP, (b) 0.4Pd-HAP, (c) 0.6Pd-HAP and (d) 1.0Pd-HAP.

**Table 3** Functionality of surface roughness parameters of Pd-HAP upon the content of Pd(II) substitutions involving roughness average ( $R_a$ ), root mean square roughness ( $R_q$ ), the maximum height of the roughness ( $R_t$ ), maximum roughness valley depth ( $R_v$ ), maximum roughness peak height ( $R_p$ ), an average maximum height of the roughness ( $R_{tm}$ ).

Composition	$R_a$ (nm)	$R_q$ (nm)	$R_t$ (nm)	$R_v$ (nm)	$R_p$ (nm)	$R_{tm}$ (nm)
0.0Pd-HAP	21.7	27.3	183.6	102.8	80.7	149.3
0.4Pd-HAP	30.8	38.8	259.1	121.3	137.8	211.1
0.6Pd-HAP	30.7	38.6	236.5	115.2	121.3	210.6
1.0Pd-HAP	35.3	44.3	311.1	138.9	172.2	237.4

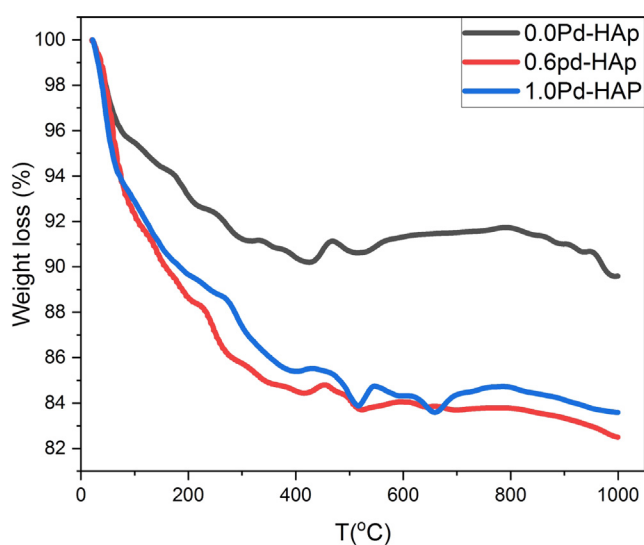


**Fig. 5** Thermogravimetric analysis of Pd-HAP upon the contributions of Pd(II) through the powder phase.

distortion, and thus promote a high tendency to destabilize, besides the high specific surface area, which encourages thermal decomposition in lower relative temperatures. Moreover, the third stage represents a plateau up to 1000 °C, whereas the samples lose around 10.4, 17.5, and 15.6% from their initial weight at 1000 °C for 0.0Pd-HAP, 0.6Pd-HAP, and 1.0Pd-HAP, respectively. The highest weight loss was recorded at 0.6Pd-HAP to be 17.5%, which might indicate relative thermal stability for the as-prepared compositions.

### 3.5. BET isotherm

The minimization of the usage doses of an antibacterial agent is pivotal for reducing the environmental loading. The increase of the effective surface could permit the use of low concentrations of the same composition, which could be accomplished by reducing the size of particles. The calculated surface area was around 28.3, 42.0, and 63.4 m<sup>2</sup>/g for 0.0Pd-HAP, 0.6Pd-HAP, and 1.0Pd-HAP, respectively as mentioned in Table 4. The total pore volume increases from 19 × 10<sup>9</sup> to 43 × 10<sup>9</sup> m<sup>3</sup>/g, while the average pore radius grows from 1.82 reaching 1.97 nm for the lowest and the highest Pd(II) contributions.

**Table 4** Nitrogen gas adsorption and desorption factors of Pd-HAP upon the content of Pd(II) involving surface area, total pore volume, and average pore radius.

Composition	Surface area (m <sup>2</sup> /g)	Total pore volume (m <sup>3</sup> /g) × 10 <sup>9</sup>	Average pore radius (nm)
0.0Pd-HAP	28.3	19	1.82
0.6Pd-HAP	42.00	28	1.91
1.0Pd-HAP	63.4	43	1.97

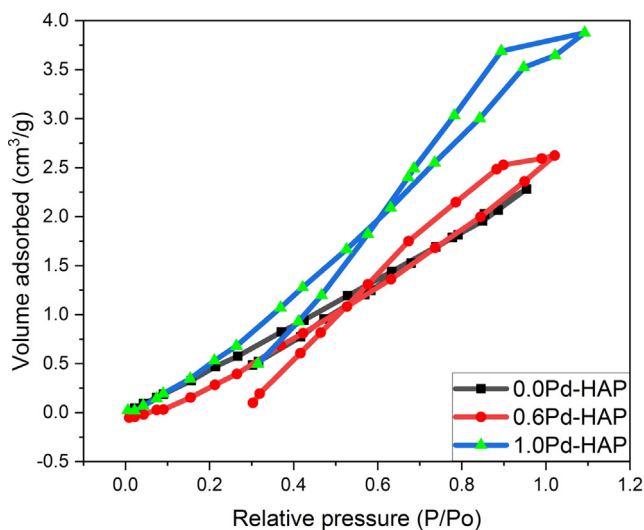


**Fig. 6** The N<sub>2</sub> adsorption/desorption isotherms behaviors of Pd-HAP upon the changing of Pd(II) ions.

The average values of pore size indicate that porosity could be classified as micro-porous compositions. As noticed from Fig. 6, the N<sub>2</sub> adsorption/desorption isotherms behaviors of Pd-HAP denote the slope of the absorbance curve increases from the low to the high Pd(II) concentrations. This behavior matches well with the results from XRD and FESEM that Pd (II) acting as a crumbling factor within HAP crystals, and thus might reduce grains size, increase porosity, and consequently promote activity. Furthermore, it could be noticed from the obtained hysteresis loops that incorporation of Pd(II) ions into HAP lattice has caused a transition of microporous structure. Thus, the surface area was enlarged upon the additional Pd (II).

### 3.6. Anti-bacterial activity

The ability of Pd-HAP to degenerate bacterial cells was investigated against both *E. coli* and *S. aureus* (gram-positive) as illustrated in Fig. 7(a)–(c). The control sample was considered to be a bacterial colony without additional antibacterial substances. The pristine HAP does not show an antibacterial effect, however, elevating Pd(II) contribution induced growing activity, as the inhibition zone increased from  $2.2 \pm 0.4$ ,  $2.6 \pm 0.6$  mm reaching to the largest area of  $4.3 \pm 0.9$  and  $4.5 \pm 0.8$  mm against both *E. coli* and *S. aureus* for

0.4Pd-HAP and 1.0Pd-HAP, respectively. The rising activity of the Pd-HAP could be assigned to the ionic release of Pd (II) through the culture medium. The Pd(II) ions displayed high chemical activity towards bacterial cell walls, which may cause degeneration of bacterial growth (Gholami Derami et al., 2020). The compositions with high values of Pd(II) display significant antibacterial behavior owing to the adequate quantity of Pd(II) that could be released through the media, besides the high dissolution rate accompanied by the high level of ionic substitutions.

### 3.7. Photocatalytic investigation

HAP displays selective adsorption behavior towards versatile organic matrices; however, its morphological features, optical properties, and structural configuration control its photocatalytic activity. Photodegradation using Pd-HAP was done against MB dye under visible light at R. T as illustrated in Fig. 8(a)–(e). The MB absorption spectra decrease exponentially upon irradiation time. The calculated degradation efficiency ( $\eta$ ) of Pd-HAP reached its highest values of 26.35, 38.74, 60.34, 71.76, and 86.4 after 120 min of continuous irradiation for compositions of 0.0Pd-HAP, 0.4Pd-HAP, 0.6Pd-HAP, 0.8Pd-HAP, and 1.0Pd-HAP, respectively. On the other hand, the degeneration of dye is noticed to obey pseudo-first-order kinetics as follows (Shouei et al., 2019; Omrani and Nezamzadeh-Ejhi, 2020):

$$\ln\left(\frac{C}{C_0}\right) = K_{app}t \quad (3)$$

where  $K_{app}$  and  $t$  are the pseudo-first-order constant ( $\text{min}^{-1}$ ) and the time, respectively. Therefore, if  $\ln\left(\frac{C}{C_0}\right)$  was plotted on the y-axis, and  $t$  on the x-axis, then from the obtained line, the  $K_{app} = \text{slope}$  as mentioned in Table 5. The calculated  $K_{app}$  increases considerably from 0.0032 reaching 0.017  $\text{min}^{-1}$  for the lowest and highest additional Pd(II), while the  $R^2$  is close to unity.

The photocatalytic interaction occurs when an incident photon with sufficient energy bombard a surface of a substance with a moderate bandgap. The direct interaction between photon and electron might generate electron-hole pairs (excitations) (Reeta Mary et al., 2018). The created photoelectrons jump up to the conduction band level (C.B), while the conjugated hole moves in the valence band (V.B). Next, the created charge carriers trigger redox serial reactions against dye molecules after their surface of a substance. These reactions may begin with a break of water molecules to generate a free radical involving ( $OH^\cdot$ ) and electron, which is able to induce a formation of superoxide ( $O_2^{\cdot-}$ ), besides the hydrogen peroxide anions ( $HO_2^\cdot$ ). These obtained free radicals are responsible to degrade the targeted dye, whereas the degradation rate depends strongly on the composition of dye and the light source, besides the compositional characteristics of the photocatalyst including its bandgap and surface area (Prabhu et al., 2018).

Furthermore, the configuration of HAP crystal possesses versatile superficial charges; whereas the a-surface is rich with ( $PO_4^{3-}$ ) anions, while the c-surface is decorated with Ca(II) cations. However, the HAP has a tendency to be crystallized in c-direction; therefore, a-surface is expected to obtain a

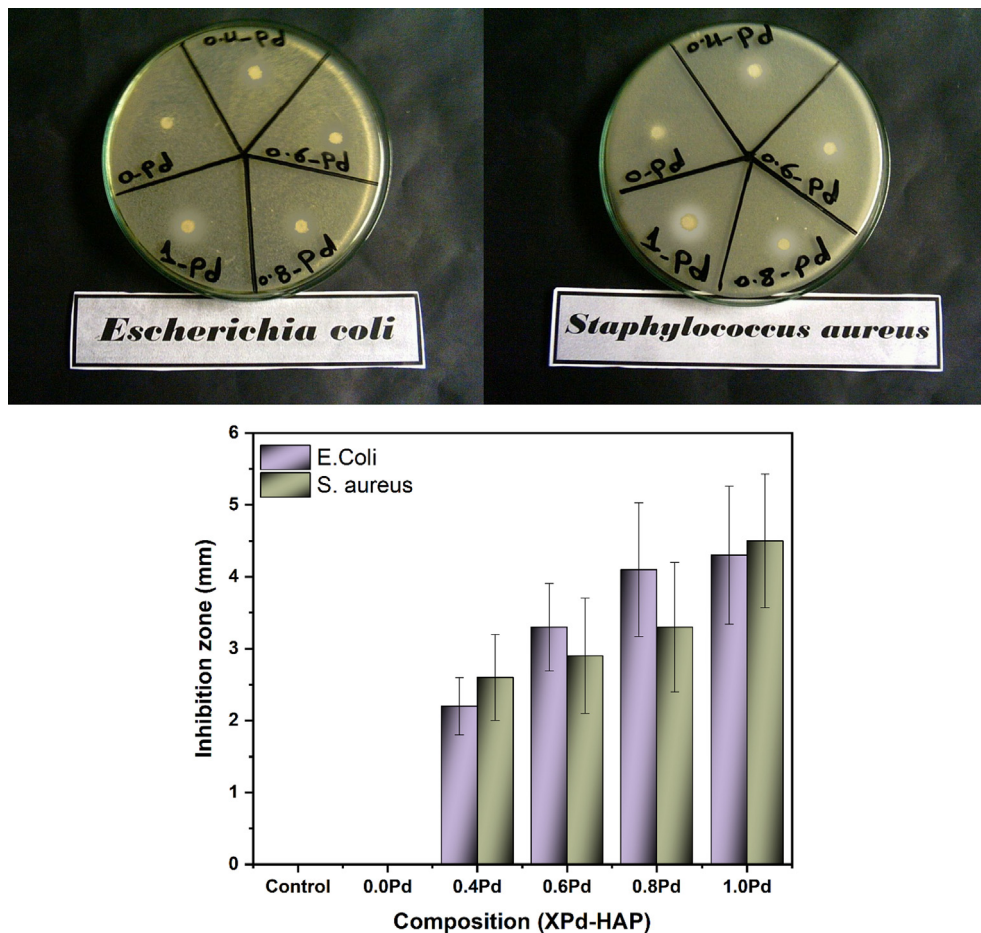
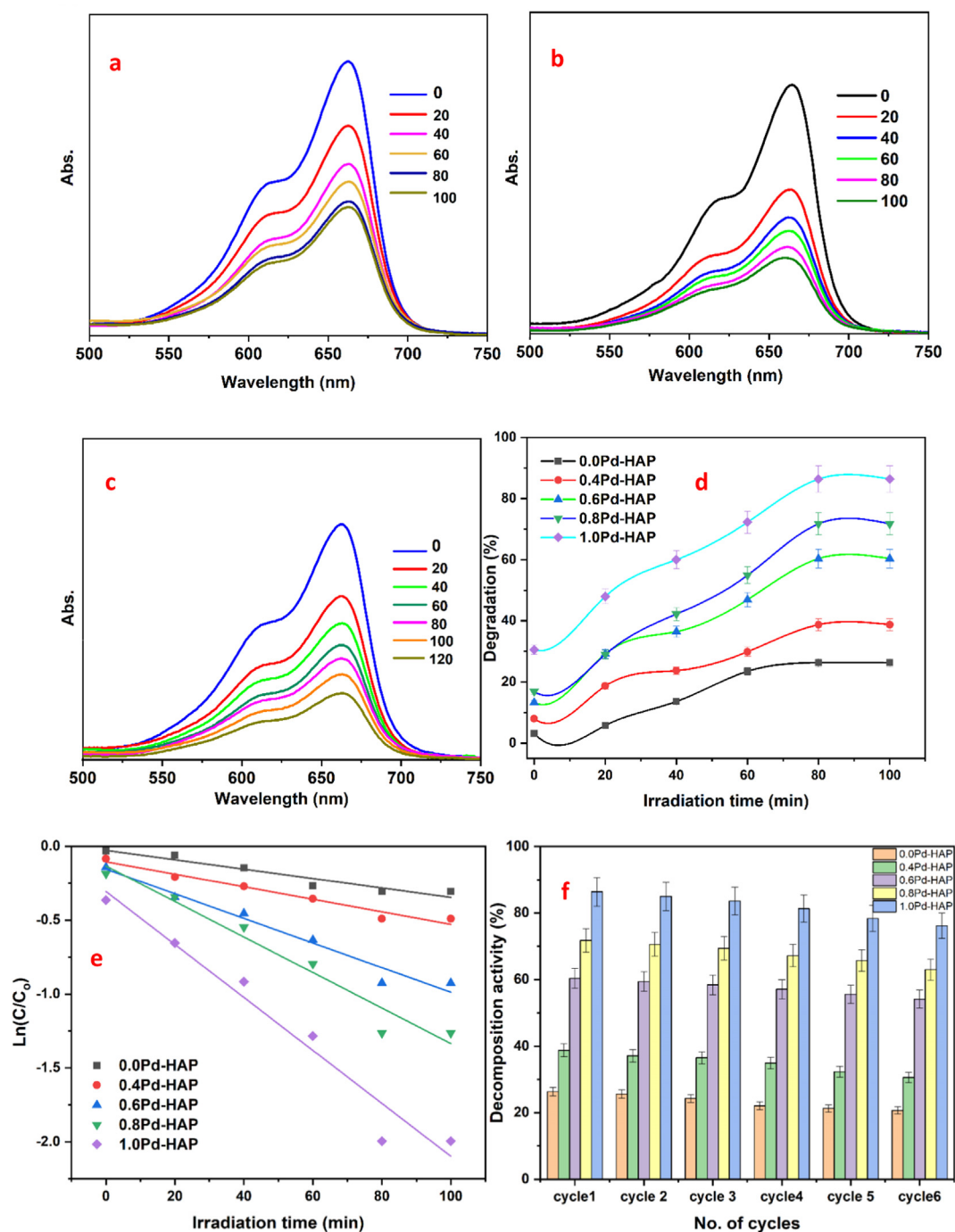


Fig. 7 Antibacterial behavior of Pd-HAP against *E. coli* and *S. aureus*.

higher surface area than c-face. Thus, the photogenerated electron through the ( $\text{PO}_4^{3-}$ ) is hypothesized to form a vacancy through HAP surface followed by a free radical generation as illustrated in Fig. 9. Hence, the dye molecules could be absorbed on the surface of HAP. Herein, it might be reported that surface roughness favors the adsorption of the dye matrix via both physical and chemical interactions (Mohseni-Salehi et al., 2018; Shoueir et al., 2020a). The chemical type is encouraged via the high content of crystallographic defects that acts as ionic traps, while the physical one is done by the adhesion on the peaks of grains. The ability to remove the agent to be reused several times represents an important economic issue. Therefore, the reusability of the Pd-HAP has been investigated for 6 cycles and showed that the removal efficiency deteriorated to be about 5.65, 8.14, 6.24, 8.76, and 10.2% for different contents of Pd(II), which indicates moderate stability for these compositions.

#### 4. Conclusion

Hydroxyapatite substituted with different contents of Pd(II) has been fabricated. The crystallized size was reduced with Pd(II) reaching 18.6 nm for the highest concentration. The estimated lattice parameters showed that the a-axis decreased from 9.447 up to 9.368, while the c-axis fluctuated from 6.875 to 6.866 for the lowest and highest contributions of Pd(II), respectively. Furthermore, the morphological variation showed that Pd-HAP was formed as agglomerated rod shapes with wide size distribution around 63.4–110.3, 44.1–59.7, 49.1–100.4, and 43.4–70.5 nm for 0.0Pd-HAP, 0.4Pd-HAP, 0.6Pd-HAP, 0.8Pd-HAP, and 1.0Pd-HAP, respectively. The roughness average ( $R_a$ ) increased from 21.7 nm reaching 35.3 nm for the lowest and highest Pd(II). Moreover, the thermogravimetric analysis showed that Pd-HAP decomposed within three stages up to 1000 °C. Finally, the weight loss reached around 10.4, 17.5, and 15.6% from their initial weight for 0.0Pd-HAP, 0.6Pd-HAP, and 1.0Pd-HAP, respectively. Besides, the antibacterial activity increased upon the additional Pd



**Fig. 8** UV-vis spectral degradation of MB towards selected (a) 0.6Pd-HAP, (b) 0.8Pd-HAP, (c) 1.0Pd-HAP, (d) kinetic model, and (d) reusability performance.

**Table 5** The pseudo-first-order constant includes  $K_{app}$  ( $\text{min}^{-1}$ ) and  $R^2$  for Pd-HAP according to their ability to remove MB dye from aqueous solutions.

Composition	$K_{app}$ ( $\text{min}^{-1}$ )	$R^2$
0.0Pd-HAP	0.0032	0.925
0.4Pd-HAP	0.0042	0.966
0.6Pd-HAP	0.0083	0.965
0.8Pd-HAP	0.012	0.957
1.0Pd-HAP	0.017	0.956

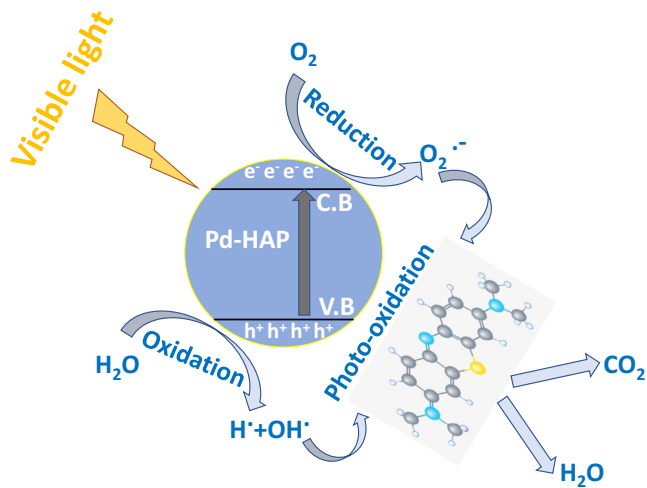


**Fig. 9** Schematic diagram of photocatalysis process to degrade MB via Pd-HAP compositions.

(II), whereas the largest inhibition zones were around  $4.3 \pm 0.9$  and  $4.5 \pm 0.8$  mm against both *E. coli* and *S. aureus*, respectively. Hence, the activity of the Pd-HAP to degenerate MB dye reached around 26.35, 38.74, 60.34, 71.76, and 86.4% after 120 min of continuous irradiation upon Pd(II) additives.

#### Declaration of Competing Interest

There is no conflict of interest.

#### References

- Abdelbar, M.F., El-Sheshtawy, H.S., Shoueir, K.R., El-Mehasseb, I., Ebeid E-Zeiny, M., El-Kemary, M., 2018. Halogen bond triggered aggregation induced emission in an iodinated cyanine dye for ultra sensitive detection of Ag nanoparticles in tap water and agricultural wastewater. *RSC Adv.* 8, 24617–24626.
- Abou-Zeid, R.E., Diab, M.A., Mohamed, S.A.A., Salama, A., Aljohani, H.A., Shoueir, K.R., 2018. Surfactant-assisted poly(lactic acid)/cellulose nanocrystal bionanocomposite for potential application in paper coating. *J. Renew. Mater.* 6, 394–401.
- Afifi, M., Ahmed, M.K., Fathi, A.M., Uskokovic, V., 2020. Physical, electrochemical and biological evaluations of spin-coated epsilon-polycaprolactone thin films containing alumina/graphene/carbonated hydroxyapatite/titania for tissue engineering applications. *Int. J. Pharm.*, 119502.
- Ahmed, M.A., Mansour, S.F., El-dek, S.I., Abd-Elwahab, S.M., Ahmed, M.K., 2014. Characterization and annealing performance of calcium phosphate nanoparticles synthesized by co-precipitation method. *Ceram. Int.* 40, 12807–12820.
- Ahmed, M.K., Mansour, S.F., Mostafa, M.S., Darwesh, R., El-dek, S. I., 2018. Structural, mechanical and thermal features of Bi and Sr co-substituted hydroxyapatite. *J. Mater. Sci.* 54, 1977–1991.
- Ahmed, M.K., Ramadan, R., El-dek, S.I., Uskoković, V., 2019a. Complex relationship between alumina and selenium-doped carbonated hydroxyapatite as the ceramic additives to electrospun polycaprolactone scaffolds for tissue engineering applications. *J. Alloy. Compd.* 801, 70–81.
- Ahmed, M.K., Mansour, S.F., Al-Wafi, R., El-dek, S.I., Uskoković, V., 2019b. Tuning the mechanical, microstructural, and cell adhesion properties of electrospun  $\epsilon$ -polycaprolactone microfibers by doping selenium-containing carbonated hydroxyapatite as a reinforcing agent with magnesium ions. *J. Mater. Sci.* 54, 14524–14544.
- Ahmed, M.K., Mansour, S.F., Al-Wafi, R., Afifi, M., Uskokovic, V., 2020a. Gold as a dopant in selenium-containing carbonated hydroxyapatite fillers of nanofibrous epsilon-polycaprolactone scaffolds for tissue engineering. *Int. J. Pharm.* 577, 118950.
- Ahmed, M.K., Mansour, S.F., Al-Wafi, R., Anter, A., 2020b. Composition and design of nanofibrous scaffolds of Mg/Se-hydroxyapatite/graphene oxide @  $\epsilon$ -polycaprolactone for wound healing applications. *J. Mater. Res. Technol.* 9, 7472–7485.
- Ahmed, M.K., Al-Wafi, R., Mansour, S.F., El-dek, S.I., Uskoković, V., 2020c. Physical and biological changes associated with the doping of carbonated hydroxyapatite/polycaprolactone core-shell nanofibers dually, with rubidium and selenite. *J. Mater. Res. Technol.*
- Ahmed, M.K., Mansour, S.F., Ramadan, R., Afifi, M., Mostafa, M.S., El-dek, S.I., et al, 2020d. Tuning the composition of new brushite/vivianite mixed systems for superior heavy metal removal efficiency from contaminated waters. *J. Water Process Eng.* 34, 101090.
- Ahmed, M.K., Menazea, A.A., Abdelghany, A.M., 2020. Blend biopolymeric nanofibrous scaffolds of cellulose acetate/epsilon-polycaprolactone containing metallic nanoparticles prepared by laser ablation for wound disinfection applications. *Int. J. Biol. Macromol.* 155, 636–644.
- Ahmed, M.K., Ramadan, R., Afifi, M., Menazea, A.A., 2020e. Au-doped carbonated hydroxyapatite sputtered on alumina scaffolds via pulsed laser deposition for biomedical applications. *J. Mater. Res. Technol.* 9, 8854–8866.
- Ahmed, M.K., Mansour, S.F., Al-Wafi, R., 2020f. Nanofibrous scaffolds of epsilon-polycaprolactone containing Sr/Se-hydroxyapatite/graphene oxide for tissue engineering applications. *Biomed. Mater.*
- Al-Wafi, R., Mansour, S.F., Ahmed, M.K., 2020. Mechanical, microstructural properties and cell adhesion of Sr/Se-hydroxyapatite/graphene/polycaprolactone nanofibers. *J. Thermoplast. Compos. Mater.* 089270572091278.
- Chen, X., Li, P., Zeng, X., Kang, Y., Wang, J., Xie, H., et al, 2020. Efficient adsorption of methylene blue by xanthan gum derivative modified hydroxyapatite. *Int. J. Biol. Macromol.* 151, 1040–1048.
- da Silva, J.S., Machado, T.R., Trench, A.B., Silva, A.D., Teodoro, V., Vieira, P.C., et al, 2020. Enhanced photocatalytic and antifungal activity of hydroxyapatite/ $\alpha$ -AgVO<sub>3</sub> composites. *Mater. Chem. Phys.* 252, 123294.
- Duta, L., Mihailescu, N., Popescu, A.C., Luculescu, C.R., Mihailescu, I.N., Çetin, G., et al, 2017. Comparative physical, chemical and biological assessment of simple and titanium-doped ovine dentine-derived hydroxyapatite coatings fabricated by pulsed laser deposition. *Appl. Surf. Sci.* 413, 129–139.
- El-dek, S.I., Mansour, S.F., Ahmed, M.A., Ahmed, M.K., 2017. Microstructural features of flower like Fe brushite. *Progr. Nat. Sci.: Mater. Int.* 27, 520–526.

- Fadeeva, I.V., Barinov, S.M., Fedotov, A.Y., Komlev, V.S., 2012. Interactions of calcium phosphates with chitosan. *Dokl. Chem.* 441, 387–390.
- Gholami Derami, H., Gupta, P., Gupta, R., Rathi, P., Morrissey, J.J., Singamaneni, S., 2020. Palladium nanoparticle-decorated mesoporous polydopamine/bacterial nanocellulose as a catalytically active universal dye removal ultrafiltration membrane. *ACS Appl. Nano Mater.* 3, 5437–5448.
- Gore, S.K., Jadhav, S.S., Jadhav, V.V., Patange, S.M., Naushad, M., Mane, R.S., et al., 2017. The structural and magnetic properties of dual phase cobalt ferrite. *Sci. Rep.* 7, 2524.
- Jiang, M., Terra, J., Rossi, A.M., Morales, M.A., Baggio Saitovitch, E.M., Ellis, D.E., 2002. Fe<sup>2+</sup>/Fe<sup>3+</sup> substitution in hydroxyapatite: theory and experiment. *Phys. Rev. B* 66.
- Lukić, M.J., Veselinović, L., Stevanović, M., Nunić, J., Dražić, G., Marković, S., et al., 2014. Hydroxyapatite nanopowders prepared in the presence of zirconium ions. *Mater. Lett.* 122, 296–300.
- Mansour, S.F., El-dek, S.I., Ahmed, M.A., Abd-Elwahab, S.M., Ahmed, M.K., 2015. Effect of preparation conditions on the nanostructure of hydroxyapatite and brushite phases. *Appl. Nanoscience* 6, 991–1000.
- Mansour, S.F., El-dek, S.I., Ahmed, M.K., 2017a. Tailoring the structure of biphasic calcium phosphate via synthesis procedure. *Mater. Res. Express* 4, 125015.
- Mansour, S.F., El-Dek, S.I., Ahmed, M.K., 2017b. Physico-mechanical and morphological features of zirconia substituted hydroxyapatite nano crystals. *Sci. Rep.* 7, 43202.
- Mansour, S.F., El-dek, S.I., Dorozhkin, S.V., Ahmed, M.K., 2017c. Physico-mechanical properties of Mg and Ag doped hydroxyapatite/chitosan biocomposites. *New J. Chem.* 41, 13773–13783.
- Mansour, S.F., El-dek, S.I., Ismail, M., Ahmed, M.K., 2018. Structure and cell viability of Pd substituted hydroxyapatite nano particles. *Biomed. Phys. Eng. Express* 4, 045008.
- Menazea, A.A., Abdelbadie, S.A., Ahmed, M.K., 2020. Manipulation of AgNPs coated on selenium/carbonated hydroxyapatite/ $\epsilon$ -polycaprolactone nano-fibrous via pulsed laser deposition for wound healing applications. *Appl. Surf. Sci.* 508, 145299.
- Mohseni-Salehi, M.S., Taheri-Nassaj, E., Hosseini-Zori, M., 2018. Effect of dopant (Co, Ni) concentration and hydroxyapatite compositing on photocatalytic activity of titania towards dye degradation. *J. Photochem. Photobiol., A* 356, 57–70.
- Niakan, A., Ramesh, S., Ganesan, P., Tan, C.Y., Purbolaksono, J., Chandran, H., et al., 2015. Sintering behaviour of natural porous hydroxyapatite derived from bovine bone. *Ceram. Int.* 41, 3024–3029.
- Omriani, N., Nezamzadeh-Ejehieh, A., 2020. A comprehensive study on the enhanced photocatalytic activity of Cu<sub>2</sub>O/BiVO<sub>4</sub>/WO<sub>3</sub> nanoparticles. *J. Photochem. Photobiol., A* 389, 112223.
- Piri, F., Mollahosseini, A., Khadir, A., Milani Hosseini, M., 2019. Enhanced adsorption of dyes on microwave-assisted synthesized magnetic zeolite-hydroxyapatite nanocomposite. *J. Environ. Chem. Eng.* 7.
- Prabhu, S.M., Khan, A., Hasmath Farzana, M., Hwang, G.C., Lee, W., Lee, G., 2018. Synthesis and characterization of graphene oxide-doped nano-hydroxyapatite and its adsorption performance of toxic diazo dyes from aqueous solution. *J. Mol. Liq.* 269, 746–754.
- Ramadan, R., 2019. Physical study of cobalt ferrite and its application in purification of water. *Appl. Phys. A* 125.
- Reeta Mary, I., Sonia, S., Navadeepthy, D., Mangalaraj, D., Viswanathan, C., Ponpandian, N., 2018. Surfactant-free solvothermal synthesis of hydroxyapatite nested bundles for the effective photodegradation of cationic dyes. *J. Phys. Chem. Solids* 116, 180–186.
- Reeta Mary, I., Leethiyal, R., Sekar, P., Mangalaraj, D., Viswanathan, C., Ponpandian, N., 2019. Self-assembly of nanostructured hydroxyapatite spheres for photodegradation of methylene blue dye. *Mater. Today: Proc.* 18, 1729–1734.
- Salama, A., Aljohani, H.A., Shoueir, K.R., 2018. Oxidized cellulose reinforced silica gel: new hybrid for dye adsorption. *Mater. Lett.* 230, 293–296.
- Shoueir, K., Kandil, S., El-hosainy, H., El-Kemary, M., 2019. Tailoring the surface reactivity of plasmonic Au@TiO<sub>2</sub> photocatalyst bio-based chitosan fiber towards cleaner of harmful water pollutants under visible-light irradiation. *J. Cleaner Prod.* 230, 383–393.
- Shoueir, K., Wassel, A.R., Ahmed, M.K., El-Naggar, M.E., 2020a. Encapsulation of extremely stable polyaniline onto Bio-MOF: photo-activated antibacterial and depletion of ciprofloxacin from aqueous solutions. *J. Photochem. Photobiol., A* 400, 112703.
- Shoueir, K., 2020. Green microwave synthesis of functionalized chitosan with robust adsorption capacities for Cr(VI) and/or RHB in complex aqueous solutions. *Environ. Sci. Pollut. Res.* 27, 33020–33031.
- Shoueir, K., Ahmed, M.K., Abdel Gaber, S.A., El-Kemary, M., 2020b. Thallium and selenite doped carbonated hydroxyapatite: microstructural features and anticancer activity assessment against human lung carcinoma. *Ceram. Int.* 46, 5201–5212.
- Tang, S., Tian, B., Guo, Y.-J., Zhu, Z.-A., Guo, Y.-P., 2014. Chitosan/carbonated hydroxyapatite composite coatings: fabrication, structure and biocompatibility. *Surf. Coat. Technol.* 251, 210–216.
- Toyama, T., Kameda, S., 2013. Synthesis of sulfate-ion-substituted hydroxyapatite from amorphous calcium phosphate. *Bioceram. Develop. Appl.* 3, 1–3.
- Wang, Z., Bai, X., 2020. One-pot synthesis of bio-supported Pd nanoparticles by using clove leaf and their catalytic performance for Suzuki coupling reaction. *J. Mol. Struct.* 1219, 128538.
- Wang, Y., Shi, L., Gao, L., Wei, Q., Cui, L., Hu, L., et al., 2015. The removal of lead ions from aqueous solution by using magnetic hydroxypropyl chitosan/oxidized multiwalled carbon nanotubes composites. *J. Colloid Interface Sci.* 451, 7–14.
- Wang, Y., Hao, H., Zhang, S., 2016. Lysozyme loading and release from Se doped hydroxyapatite nanoparticles. *Mater. Sci. Eng. C, Mater. Biol. Appl.* 61, 545–552.
- Wang, Y., Hu, L., Zhang, G., Yan, T., Yan, L., Wei, Q., et al., 2017a. Removal of Pb(II) and methylene blue from aqueous solution by magnetic hydroxyapatite-immobilized oxidized multi-walled carbon nanotubes. *J. Colloid Interface Sci.* 494, 380–388.
- Wang, Y., Hao, H., Zhang, S., 2017b. Biomimetic coprecipitation of silk fibrin and calcium phosphate: influence of selenite ions. *Biol. Trace Elem. Res.* 178, 338–347.
- Wang, Y., He, W., Hao, H., Wu, J., Qin, N., 2018. Eggshell derived Se-doped HA nanorods for enhanced antitumor effect and curcumin delivery. *J. Sol-Gel Sci. Technol.* 87, 600–607.
- Wang, Z., Gao, M., Li, X., Ning, J., Zhou, Z., Li, G., 2020a. Efficient adsorption of methylene blue from aqueous solution by graphene oxide modified persimmon tannins. *Mater. Sci. Eng. C, Mater. Biol. Appl.* 108, 110196.
- Wang, Y., Zhao, G., Wang, H., Zhang, Y., Zhang, N., Wei, D., et al., 2020b. Label-free electrochemical immunosensor based on biocompatible nanoporous Fe<sub>3</sub>O<sub>4</sub> and biotin-streptavidin system for sensitive detection of zearalenone. *The Analyst* 145, 1368–1375.
- Wang, Y., Bi, N., Zhang, H., Tian, W., Zhang, T., Wu, P., et al., 2020c. Visible-light-driven photocatalysis-assisted adsorption of azo dyes using Ag<sub>2</sub>O. *Colloids Surf., A* 585, 124105.
- Wu, V.M., Ahmed, M.K., Mostafa, M.S., Uskoković, V., 2020a. Empirical and theoretical insights into the structural effects of selenite doping in hydroxyapatite and the ensuing inhibition of osteoclasts. *Mater. Sci. Eng., C* 111257.
- Wu, Z., Huang, W., Shan, X., Li, Z., 2020b. Preparation of a porous graphene oxide/alkali lignin aerogel composite and its adsorption properties for methylene blue. *Int. J. Biol. Macromol.* 143, 325–333.
- Xu, J., Du, P., Bi, W., Yao, G., Li, S., Liu, H., 2020. Graphene oxide aerogels co-functionalized with polydopamine and polyethyleneimine for the adsorption of anionic dyes and organic solvents. *Chem. Eng. Res. Des.* 154, 192–202.

- Xu, Q., Owens, G., Chen, Z., 2020. Adsorption and catalytic reduction of rifampicin in wastewaters using hybrid rGO@Fe/Pd nanoparticles. *J. Cleaner Prod.* 264, 121617.
- Yao, G., Bi, W., Liu, H., 2020. pH-responsive magnetic graphene oxide/poly(NVI-co-AA) hydrogel as an easily recyclable adsorbent for cationic and anionic dyes. *Colloids Surf., A* 588, 124393.
- Yilmaz, V.T., Icel, C., Turgut, O.R., Aygun, M., Evren, E., Ozdemir, I., 2020. Synthesis, structures and catalytic activity of Pd(II) saccharinate complexes with monophosphines in direct arylation of five-membered heteroarenes with aryl bromides. *Inorg. Chim. Acta* 500, 119220.
- Zhang, W., Xu, X., Chai, Y., Wang, Y., 2016. Synthesis and characterization of  $Zn^{2+}$  and  $SeO_3^{2-}$  co-substituted nano-hydroxyapatite. *Adv. Powder Technol.*
- Zhang, Q., Cheng, Y., Fang, C., Chen, J., Chen, H., Li, H., et al, 2020a. Facile synthesis of porous carbon/Fe<sub>3</sub>O<sub>4</sub> composites derived from waste cellulose acetate by one-step carbothermal method as a recyclable adsorbent for dyes. *J. Mater. Res. Technol.*
- Zhang, Q.Q., Zhu, Y.J., Wu, J., Shao, Y.T., Dong, L.Y., 2020b. A new kind of filter paper comprising ultralong hydroxyapatite nanowires and double metal oxide nanosheets for high-performance dye separation. *J. Colloid Interface Sci.* 575, 78–87.
- Zhao, J., Wang, C., Wang, S., Zhou, Y., Zhang, B., 2020a. Experimental and DFT studies on the selective adsorption of Pd (II) from wastewater by pyromellitic-functionalized poly(glycidyl methacrylate) microsphere. *J. Mol. Liq.* 300, 112296.
- Zhao, B., Zhu, Z., Qin, X.D., Li, Z., Zhang, H., 2020b. Highly efficient and stable CuZr-based metallic glassy catalysts for azo dye degradation. *J. Mater. Sci. Technol.* 46, 88–97.
- Zheng, X., Dong, Y., Liu, T., 2020. Simultaneous photodegradation of dyes by NiS/CuS-CdS composites in visible light region. *Colloids Surf., A* 598, 124854.
- Zhu, M., Liu, Y., Chen, M., Gan, D., Wang, M., Zeng, H., et al, 2020. Ultrahigh flux of graphene oxide membrane modified with orientated growth of MOFs for rejection of dyes and oil-water separation. *Chin. Chem. Lett.*
- Zou, L., Wang, H., Jiang, X., Yuan, G., Wang, X., 2020. Enhanced photocatalytic efficiency in degrading organic dyes by coupling CdS nanowires with ZnFe<sub>2</sub>O<sub>4</sub> nanoparticles. *Sol. Energy* 195, 271–277.